

Suzaku Detection of Thermal X-Ray Emission Associated with the Western Radio Lobe of Fornax A

Hiromi SETA¹, Makoto S. TASHIRO², and Susumu INOUE³

¹*Research Center for Measurement in Advanced Science, Faculty of Science, Rikkyo University 3-34-1
Nishi-Ikebukuro, Toshima-ku, Tokyo Japan 171-8501
seta@rikkyo.ac.jp*

²*Department of Physics, Saitama University, 255 Shimo-Okubo, Sakura-ku, Saitama Japan 338-8570*

³*Max-Planck-Institut für Kernphysik, Saupfercheckweg 1, 69117 Heidelberg Germany*

(Received 2013 May 4; accepted 2013 July 1)

Abstract

We present the results of X-ray mapping observations of the western radio lobe of the Fornax A galaxy, using the X-ray Imaging Spectrometer (XIS) onboard the Suzaku satellite with a total exposure time of 327 ks. The purpose of this study is to investigate the nature and spatial extent of the diffuse thermal emission around the lobe by exploiting the low and stable background of the XIS. The diffuse thermal emission had been consistently reported in all previous studies of this region, but its physical nature and relation to the radio lobe had not been examined in detail. Using the data set covering the entire western lobe and the central galaxy NGC 1316, as well as comparison sets in the vicinity, we find convincingly the presence of thermal plasma emission with a temperature of ~ 1 keV in excess of conceivable background and contaminating emission (cosmic X-ray background, Galactic halo, intra-cluster gas of Fornax, interstellar gas of NGC 1316, and the ensemble of point-like sources). Its surface brightness is consistent with having a spherical distribution peaking at the center of the western lobe with a projected radius of $\sim 12'$. If the volume filling factor of the thermal gas is assumed to be unity, its estimated total mass amounts to $\sim 10^{10} M_{\odot}$, which would be $\sim 10^2$ times that of the central black hole and comparable to that of the current gas mass of the host galaxy. Its energy density is comparable to or larger than those in the magnetic field and non-thermal electrons responsible for the observed radio and X-ray emission.

Key words: galaxies: individual (Fornax A) – galaxies: magnetic fields – radiation mechanisms: non-thermal – radio continuum: galaxies – X-rays: galaxies

1. Introduction

Radio galaxies exhibit powerful outflows of magnetized plasma that emanate as collimated jets from their nuclei and end in extended structures known as lobes. The jets and lobes are most prominently observed in the radio band through the synchrotron emission of relativistic electrons that are accelerated at different locations in the outflow. Although the jets are believed to be powered by the super-massive black hole residing in the nucleus of the host galaxy, the basic physical mechanisms that drive their formation and evolution are still poorly understood. The lobes are thought to result from the interaction of the outflow with the external intergalactic or intra-cluster medium (ICM), whereby the kinetic energy of the jets is dissipated and their momentum isotropized (e.g. Begelman et al. 1984). It has become increasingly apparent in recent years that these lobes also constitute the interface through which jets strongly influence the evolution of their host galaxies, groups, and/or clusters by heating and redistributing the ambient gas in different ways. However, the actual physical processes responsible for such effects are currently under intensive debate (McNamara & Nulsen 2007; McNamara & Nulsen 2012). Detailed studies of the composition and energy balance

of different components inside the lobes of radio galaxies should therefore provide valuable insight into the physics of not only the jets themselves, but also of feedback effects that are crucial for the evolution of large-scale structure in the Universe.

Fornax A (NGC 1316; hereafter For A) is one of the closest and brightest radio galaxies, which is known to have a distinctive, two-sided lobe structure. It is the brightest in the GHz band (Ekers et al. 1983), and was the first to be reported to have diffuse, non-thermal X-ray emission, which is generated by inverse Compton up-scattering of ambient radiation (primarily the cosmic microwave background; Feigelson et al. 1995; Kaneda et al. 1995). Since then, many other radio galaxies have been observed with X-ray emission from large-scale jets (Harris & Krawczynski 2006). Although For A can be considered to be an archetypal object for non-thermal X-ray emitting lobes, it is somewhat atypical in the internal energy balance. The ratio of the energy densities in non-thermal electrons and the magnetic field, as estimated from the relative strengths of the inverse Compton and synchrotron emission, is exceptionally low compared to the lobes of other objects (Isobe et al. 2009). This may be somehow related to the unique evolutionary state of For A; the unusually low X-ray luminosity of the nucleus of its host

galaxy NGC 1316 (5×10^{39} erg s $^{-1}$ in 0.3–8.0 keV; Kim & Fabbiano 2003) suggests that the central black hole ceased its activity some 0.1 Gyr ago from Iyomoto et al. 1998 (See also Lanz et al. 2010). Emission from such relic radio lobes whose power supply has been switched off are expected to fade away not long afterwards, as the residual non-thermal electrons will only cool via radiative and Coulomb losses.

For most radio galaxies, observations up to now have indicated that their lobes do not contain a significant amount of thermal material (McNamara & Nulsen 2007). For A stands out as a unique sample in its apparent existence of diffuse thermal X-ray emission around its lobes. In addition to the diffuse non-thermal X-ray emission of inverse Compton origin, all previous X-ray studies have consistently suggested that thermal emission is also present in the spectra for both lobes on either side of the nucleus (Feigelson et al. 1995; Kaneda et al. 1995; Tashiro et al. 2001; Isobe et al. 2006; Tashiro et al. 2009). This thermal emission had been ascribed to hot gas of either the Fornax cluster or around the NGC 1316 galaxy. However, the alternative possibility that the emission actually originates from within the radio lobes had not been seriously investigated, due to the lack of spatially-resolved X-ray spectroscopy with low-background covering the entire lobe structure. Of further interest is the recent, possible detection of diffuse thermal emission in the giant, outer lobes of the Centaurus A (hereafter Cen A) radio galaxy using the Suzaku satellite (Stawarz et al. 2013).

In this paper, we revisit the issue of diffuse thermal emission around the For A radio lobe. We present the results of the first X-ray mapping observations to cover the entire western lobe of For A, with an extent of 20' in diameter, as well as its surroundings to examine the presence of the diffuse thermal emission and its association with the radio lobe.

The plan of this paper is as follows. In § 2, we describe the Suzaku mapping observations of the western lobe and their data reduction. In § 3, we present the X-ray image (§ 3.1) and spectra, for which we evaluate the contributions of various conceivable sources of background and contaminating emission (§ 3.2 and 3.3). We conclude that the diffuse thermal emission does originate from within the lobe and investigate its spatial distribution (§ 3.4). In § 4, we derive the total mass and energy of the diffuse gas and compare it with other forms of energy, as well as with the results for the Cen A outer lobe (Stawarz et al. 2013; O'Sullivan et al. 2013). We summarize the main findings of this paper in § 5.

Throughout this paper, we assume a distance of 18.6 Mpc and a redshift of 4.65×10^{-3} for For A (Madore et al. 1999). We evaluate the observed surface brightness of the diffuse emission in units of erg s $^{-1}$ cm $^{-2}$ str $^{-1}$, without correcting for Galactic absorption and assuming a uniform projected distribution, unless otherwise noted. Fiducial energy bands of 0.5–2.0 keV and 2.0–10.0 keV are chosen as typical ranges for the thermal and non-thermal components, respectively.

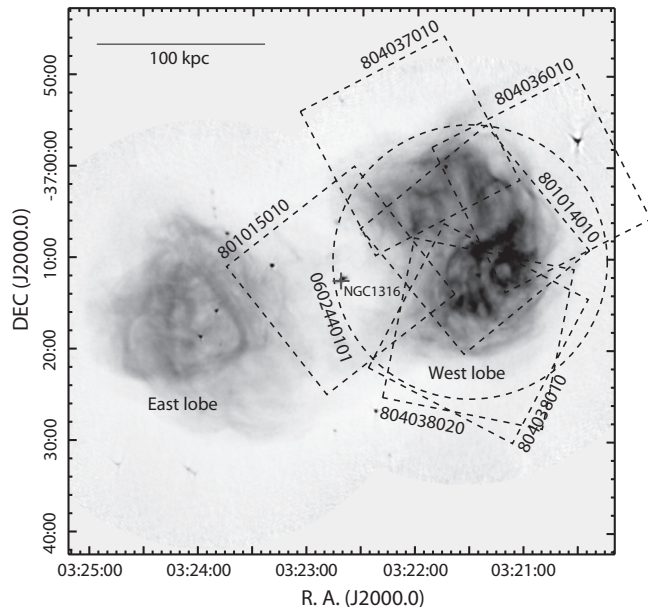


Fig. 1. Mapping layout of the Suzaku observations overlaid on a 1.5 GHz radio intensity map in gray scale (Fomalont et al. 1989). The Suzaku XIS and XMM-Newton MOS fields of view are shown as dashed squares and circles, respectively, with the sequence ID labels as in table 1. The position of the nucleus of NGC 1316 is shown with a cross.

2. Observations & Data Reduction

We performed six mapping observations of the western lobe of For A using the Suzaku satellite (Mitsuda et al. 2007). Suzaku has two kinds of operational instruments; the X-ray Imaging Spectrometer (XIS; Koyama et al. 2007) and the non-imaging Hard X-ray Detector (Kokubun et al. 2007; Takahashi et al. 2007). We concentrate on the XIS data in this paper, because we focus on the spatial distribution of the thermal emission around the lobe.

The mapping layout is shown in figure 1, while the observation details are summarized in table 1. Two observations were made in 2006 and the remaining four in 2009. The data for the central part of the western lobe in the earlier observation (sequence ID 801014010 in figure 1) has already been presented in Tashiro et al. (2009). In this paper, we assembled the additional data sets taken in the flanking fields to complete the coverage of the western lobe and the central galaxy (NGC 1316) of For A with a total exposure time of 327 ks.

The XIS is equipped with four X-ray charge coupled devices (CCDs) placed at the focus of four independent and co-aligned X-ray telescopes (Serlemitsos et al. 2007). The instrument provides X-ray imaging-spectroscopic capability in the 0.2–12 keV band. Three devices (XIS0, 2 and 3) are front-illuminated (FI), while the remaining one (XIS1) is back-illuminated (BI). The FI and BI sensors have comparatively better response in the hard and soft X-ray bands, respectively. The entire XIS2 and part of the XIS0 became dysfunctional due to putative micro-

Table 1. Suzaku and XMM-Newton data sets for For A.

Observatory	Sequence ID	Aiming position (J2000.0)		Observation	t_{exp}^*
		R. A.	DEC	start date	(ks)
Suzaku	801015010	03 ^h 22 ^m 40 ^s .4	−37°12′10″	2006-12-22	86.7
	801014010	03 ^h 21 ^m 40 ^s .4	−37°09′52″	2006-12-23	42.9
	804036010	03 ^h 20 ^m 53 ^s .3	−37°02′03″	2009-06-08	54.8
	804037010	03 ^h 22 ^m 05 ^s .5	−37°58′03″	2009-06-09	55.5
	804038010	03 ^h 21 ^m 25 ^s .9	−37°18′39″	2009-06-30	47.0
	804038020	03 ^h 21 ^m 25 ^s .7	−37°18′40″	2009-08-02	39.6
XMM-Newton	0602440101	03 ^h 21 ^m 29 ^s .3	−37°11′30″	2009-06-25	59.5

* The mean exposure time of the three XIS sensors for Suzaku and the two MOS and one PN sensors for XMM-Newton.

meteorite hits since 2006 November and 2009 June, respectively, and we used the remaining parts of the devices. The XIS covers an 18′×18′ field with a telescope half-power diameter of ∼2′. Two radioactive ⁵⁵Fe sources illuminate two corners of each device for calibration purposes. The total effective area and the energy resolution in full width at half maximum (FWHM) are 300 cm² and ∼ 170 eV at 6 keV for FI, and 250 cm² and ∼ 200 eV at 6 keV for BI, respectively. We operated the XIS in the normal clocking mode with a frame time of 8 s in all observations. The relatively large effective area and arguably the lowest and most stable instrumental background among all previous X-ray CCD instruments in orbit give the XIS an advantage in investigating diffuse X-ray emission with low surface brightness, such as the subject of this study.

We retrieved the pipeline products and processed the data using the HEADAS software package¹ version 6.12 and the latest calibration database (CALDB) as of writing. We removed events taken during passages over the South Atlantic Anomaly, those with elevation angles below 20 and 5 degrees from the day and night Earth, respectively, and with the ASCA grades 1, 5, and 7. The net exposure times are given in table 1.

We also retrieved the archival XMM-Newton data (Nulsen et al. 2011; Panagoulia et al. 2011) to supplement the Suzaku data for investigating point-like X-ray sources that are potential contamination for the diffuse emission of our interest. We found one data set centered at the western lobe (figure 1). The XMM-Newton satellite (Jansen et al. 2001) carries three X-ray instruments. We used the data taken with the two imaging-spectroscopic instruments: the European Photon Imaging Camera (EPIC) MOS (Turner et al. 2001) and PN (Strüder et al. 2001).

3. Analysis & Results

3.1. X-ray Images

Figure 2 shows the (a) mosaicked XIS and (b) MOS images. The XIS image is shown in the 0.67–1.5 keV band in logarithmic scale to focus on the diffuse emission from thermal plasma with a temperature of $k_{\text{B}}T \sim 1$ keV as reported in previous work (Feigelson et al. 1995; Kaneda et al. 1995; Tashiro et al. 2001; Tashiro et al. 2009),

whereas the MOS image is in the 0.2–10 keV band in linear scale to highlight point-like sources.

Numerous point-like sources are recognized in the MOS image with the brightest one being the nucleus of NGC 1316. Another bright point-like source is found in the northwest quadrant of the western lobe, which is an unidentified source (XMMU J032112.4–370337). Besides these point-like sources, it is evident that diffuse emission exists in the XIS image. The surface brightness distribution of the diffuse emission suggests that there are two spatially distinct components: one is centered at NGC 1316 (hereafter called “the galaxy component”), and the other is in the western lobe (“the lobe component”). To characterize the X-ray spectrum of the latter, we define the “lobe region”, shown with the thick red ellipse (R3+R4) in figure 2 (a).

3.2. X-ray Spectra (1) Background Emission

As the emission of interest has a low surface brightness, we carefully subtracted the background emission. We evaluated the contribution of (1) non X-ray background (NXB; § 3.2.1), (2) celestial X-ray diffuse background seen in all directions, and (3) the possible intra-cluster gas (§ 3.2.2) by making a comparison with other regions in the Fornax cluster.

For spectral fitting, we used the XSPEC package version 12.7. We generated the redistribution matrix functions (RMF) using the `xisrmfgen` tool, and the auxiliary response files (ARF) using the `xissimarfgen` tool (Ishisaki et al. 2007). The two FI spectra with XIS0 and XIS3 were merged in view of their nearly identical responses, while the BI spectrum was treated separately. When source spectra were extracted using multiple data sets, the source and background spectra and the response files were averaged, weighted by exposure times effective area using the `addascaspec` tool. The fitting parameters were constrained to be the same between the FI and BI spectra except for a normalization factor of a few percent to account for the internal calibration uncertainties².

3.2.1. Non X-ray background

First, we considered the contribution from the NXB, which is caused mainly by charged particles interacting

¹ See <http://heasarc.gsfc.nasa.gov/lheasoft/> for detail.

² See <http://www.astro.isas.jaxa.jp/suzaku/doc/suzakumemo/suzakumemo-2008-06.pdf> for detail.

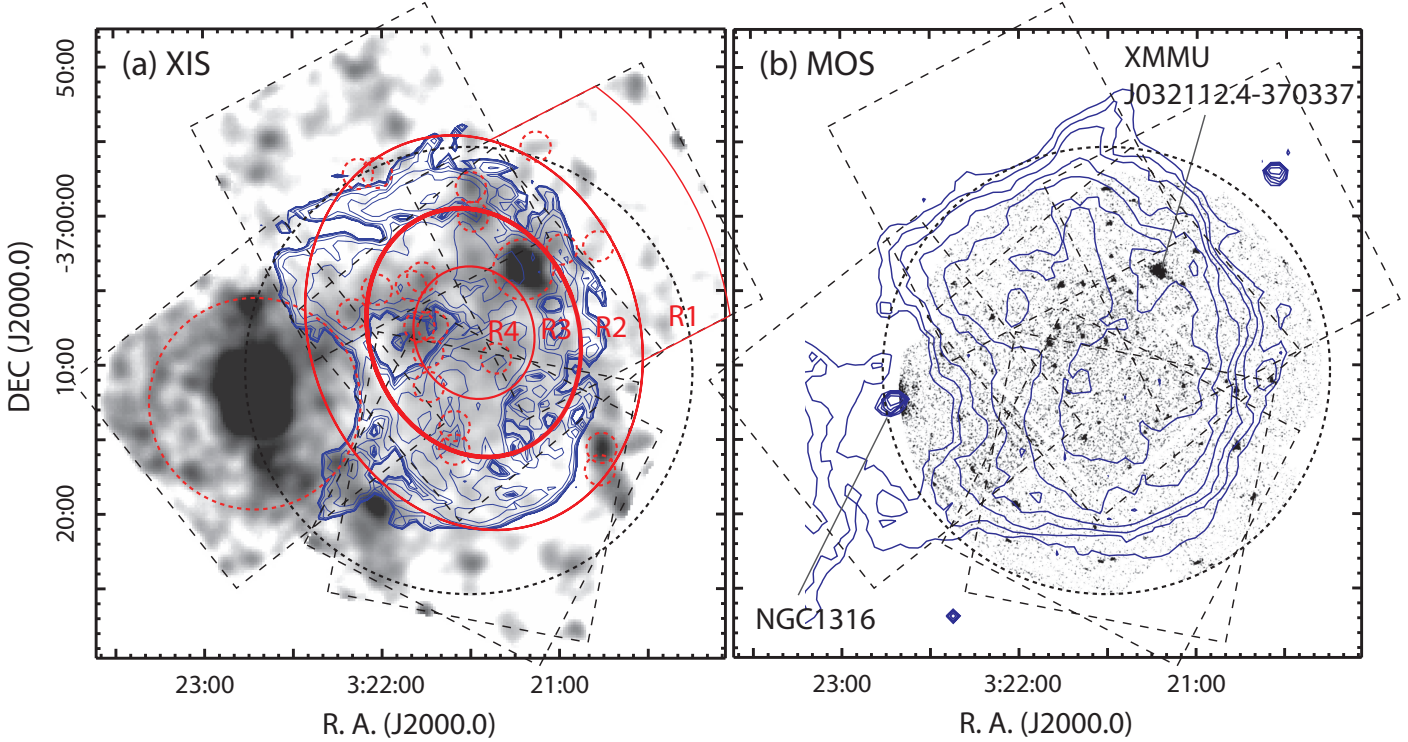


Fig. 2. (a) Suzaku XIS and (b) XMM-Newton MOS2 image of the western lobe and NGC 1316. The XIS image is shown in the 0.67–1.5 keV band in logarithmic scale to emphasize the diffuse thermal emission, while the MOS image is shown in the 0.2–10 keV band in linear scale to highlight point-like sources. The blue contours indicate (a) linear polarized and (b) total intensities at 1.5 GHz (Fomalont et al. 1989). In (a), events from the three sensors were merged, and the differences in the exposure and the effective area were corrected, and the image was smoothed by a Gaussian convolution. The source extraction regions are shown as red curves; the thick ellipse (R3+R4) for characterizing the lobe spectrum, and the concentric elliptical annuli (R2–R4) as well as the flanking region (R1) for studying the spatial distribution. The masked circles around point-like sources and the central galaxy are shown as red dashed circles. In both images, the XIS and MOS fields of view are shown respectively as the dashed squares and the circle. The background was not subtracted in the images.

with the sensors and surrounding structures, and is thus strongly correlated with the geomagnetic cut-off-rigidity of the satellite orbit at the time of observations. The level of the NXB of the XIS is so low and stable that it can be reproduced by the accumulation of non-contemporaneous data taken while the telescope is pointed toward the night Earth. Using the `xisnxbgen` tool, we simulated the NXB spectrum by accumulating the night Earth data in such a manner that the cut-off-rigidity histogram matches the actual observations. With this approach, Tawa et al. (2008) demonstrated that the NXB spectrum is reproduced at an accuracy of $\sim 5\%$ in the count rate.

For the FI spectra, we further fine-tuned the normalization of the simulated NXB spectrum using instrumental features, most notably the Ni I $K\alpha$ emission line at 7.47 keV. We derived the intensity of the emission line in both the actual and simulated spectra by phenomenologically fitting them with a power-law continuum plus a Gaussian line model in the 6.7–8 keV band. The free parameters in the model were the power-law normalization and index, and the Gaussian normalization. The center

energy and width of the Gaussian component were fixed to 7.47 keV and 0 eV, respectively. We rescaled the simulated NXB spectra so that the Ni I $K\alpha$ line intensity became equal to that of the actual data.

For the BI spectra, the approach for the FI cannot be taken as the NXB level is much higher in the high energy end of the spectrum including the Ni I $K\alpha$ line. Instead, we used the count rate in the 8–10 keV range to derive the rescaling factor, where the NXB emission dominates over the celestial X-ray emission.

3.2.2. Celestial X-ray diffuse background

For the celestial background emission seen in any direction of the sky, two sources make major contributions in the energy range and the surface brightness that we study: (1) the Galactic halo emission, which is characterized by optically-thin thermal plasma emission with a temperature of 0.2–0.4 keV and a surface brightness of $\approx 10^{-8}$ erg s $^{-1}$ cm $^{-2}$ str $^{-1}$ (Lumb et al. 2002) and (2) the cosmic X-ray background (CXB) emission, which is characterized by a power-law spectrum with a photon index of ~ 1.4 and a surface brightness of

$\approx 10^{-7.5}$ erg s $^{-1}$ cm $^{-2}$ str $^{-1}$ (Kushino et al. 2002). In addition, there should be diffuse emission pervasive in the Fornax cluster that NGC 1316 belongs to.

We evaluated the contribution of these components by making a comparison with other XIS data in near-by fields. For A is displaced from the cluster center by 3.6° , and we retrieved the archival data taken at similar cluster-centric distances. Three data sets devoid of bright point-like sources were found (table 2). All the data were taken with the normal clocking mode.

We identified point-like sources in the XIS images (0.5–5.5 keV) for the For A region and the three comparison regions using the sliding cell technique in the XIMAGE package. We masked a circle of $1'$ in radius around these sources. In addition, for a few bright sources including XMMU J032112.4–370337, we expanded the masking radius up to $2'$ so that the events spilled outside of the masks are negligible in comparison to the background events. We also masked the region within $7'$ around NGC 1316. The masked regions are shown as the red dashed circles in figure 2 (a) for the For A region.

We fitted the NXB-subtracted spectra with a model consisting of the Galactic halo and the CXB components. For the Galactic halo component, we used the APEC model (Smith et al. 2001) with the plasma temperature ($k_B T^{(\text{GH})}$) and the surface brightness ($S^{(\text{GH})}$) as free parameters and the metal abundance fixed to that of solar (Anders & Grevesse 1989). For the CXB component, we used the power-law model with the surface brightness ($S^{(\text{CXB})}$) as a free parameter and the power-law index fixed to 1.4 (Kushino et al. 2002). These components were attenuated by an interstellar photo-electric absorption model with an absorption column fixed to the Galactic value toward each region (Kalberla et al. 2005).

Figure 3 shows the spectra and the best-fit models, while table 3 summarizes the best-fit parameters. The spectra in the three comparison regions were well fitted by the Galactic halo plus CXB model. All the parameters are consistent with the previous studies in different regions (Lumb et al. 2002; Kushino et al. 2002; Yoshino et al. 2009). No additional component was required, suggesting that the diffuse thermal emission in the Fornax cluster, if any, does not make a significant contribution at such large cluster-centric distances. This is consistent with the ROSAT result (Jones et al. 1997), in which the radial profile of the surface brightness of the Fornax cluster gas was presented out to 280 kpc ($\sim 40'$) from the cluster center. The observed value at 200 kpc is 1×10^{-8} erg s $^{-1}$ cm $^{-2}$ str $^{-1}$ and the extrapolated value at the position of Fornax A is $< 10^{-10}$ erg s $^{-1}$ cm $^{-2}$ str $^{-1}$, which is far below our detection level.

In contrast, the same model was found inadequate for the spectrum in the lobe region. The largest difference from the other three regions is the excess emission peaking at ~ 1 keV, indicating the presence of extra emission local to the lobe region as we noticed in figure 2 (a).

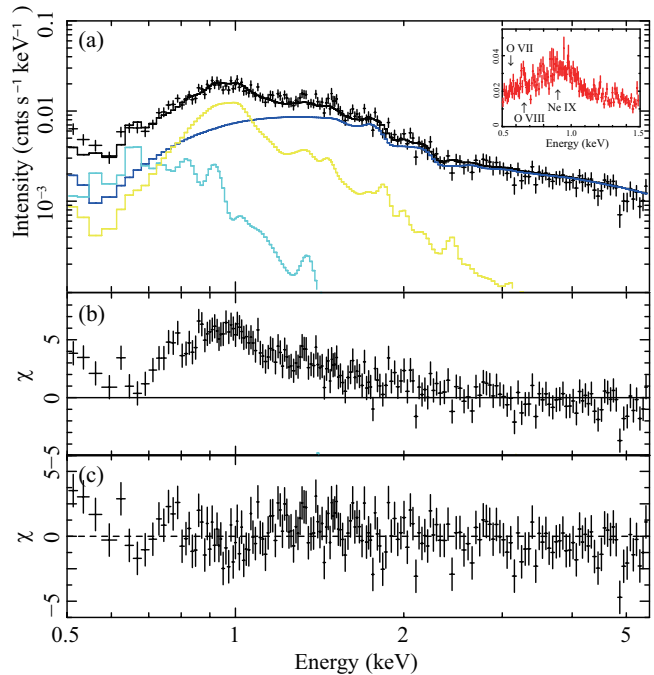


Fig. 4. Spectral fitting of the lobe emission. Only the FI results are shown for clarity unless otherwise noted. (top) The NXB-subtracted spectra and the best-fit spectral model. Each component is color-coded: yellow for the lobe thermal, cyan for the Galactic halo, and blue for the CXB. A close-up view of the BI spectrum in the soft band is given in the inset. (middle) The residuals to the fit by the model consisting only of the Galactic halo and the CXB components. (bottom) The residuals to the fit by the model consisting of the lobe thermal, Galactic halo, and the CXB components.

3.3. X-ray Spectra (2) Lobe Emission

3.3.1. Thermal emission

In a close-up view of the lobe spectrum in the soft-band (inset in the top panel in figure 4), several emission features are recognized. While the O VII and O VIII lines respectively at 0.57 and 0.65 keV are from the Galactic halo component with a temperature of $k_B T = 0.2$ keV, the Ne IX line at 0.91 keV and Fe L series lines at ~ 1 keV should be from a thermal plasma of a higher temperature.

Therefore, we added a thermal plasma component represented by the APEC model with free parameters for the plasma temperature ($k_B T^{(\text{lobe}, T)}$) and the surface brightness ($S^{(\text{lobe}, T)}$) and a fixed value of 0.3 solar for the abundance. The residuals were reduced substantially (the middle and the bottom panels in figure 4 respectively show the results without and with the additional thermal component) and yielded a statistically acceptable result. The best-fit result is summarized in table 4.

3.3.2. Contaminating emission

We next evaluated how these parameters are affected by contaminating emission that are unseen in the comparison regions: the point-like sources (§ 3.3.2.1), the non-thermal emission in the lobe (§ 3.3.2.2), and the diffuse emission associated with the central galaxy NGC 1316 (§ 3.3.2.3).

Table 2. Suzaku data sets for the comparison regions in the Fornax cluster.

Sequence ID	Position (J2000.0)		Observation start date	Dist.* (arcdeg)	t_{exp}^\dagger (ks) ^b
	R. A.	DEC			
703038010	03 ^h 31 ^m 06 ^s .3	−38°24′05″	2008-06-16	3.30	24.3
802037010	03 ^h 13 ^m 10 ^s .4	−37°40′25″	2007-06-28	5.55	15.0
802040010	03 ^h 19 ^m 57 ^s .4	−32°03′58″	2007-06-29	5.13	19.7

* The distance from the center of the Fornax cluster at (R. A., Decl.)=(03^h38^m30^s.9, −35°27′16″).

† The mean exposure time of the three XIS sensors.

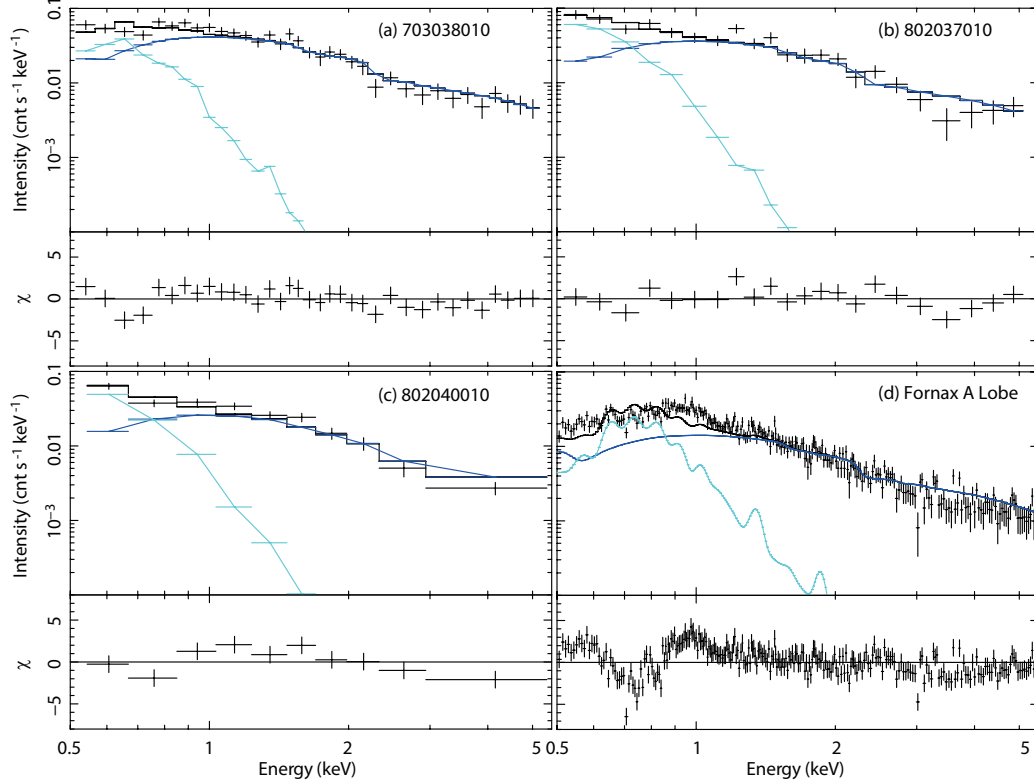


Fig. 3. Spectra and the best-fit models of the diffuse spectrum of (a)–(c) the three comparison regions and (d) the lobe region. The spectra were binned with 100 counts bin^{−1} except for (c) with 150 counts bin^{−1} to compensate for its poorer statistics. The model is composed of the Galactic halo (cyan) and CXB (blue) components. For (d), the temperature of the thermal emission was fixed to $k_{\text{B}}T = 0.2$ keV to reproduce the Galactic halo emission, rather than the lobe thermal emission.

Table 3. Fitting results for the comparison regions*†.

Region	Absorption $N_{\text{H}}/10^{20}$	Galactic halo		CXB	$\chi^2/\text{d.o.f.}$
		$k_{\text{B}}T^{(\text{GH})}$	$S^{(\text{GH})}/10^{-8}$	$S^{(\text{CXB})}/10^{-8}$	
	(1)	(2)	(3)	(4)	(5)
703038010	1.33	0.20 ^{+0.04} _{−0.01}	1.04 ^{+0.13} _{−0.13}	7.92 ^{+0.25} _{−0.25}	101.4/71
802037010	1.77	0.18 ^{+0.01} _{−0.01}	1.42 ^{+0.17} _{−0.16}	6.73 ^{+0.21} _{−0.23}	63.4/41
802040010	1.34	0.19 ^{+0.01} _{−0.01}	1.19 ^{+0.15} _{−0.14}	4.94 ^{+0.22} _{−0.22}	33.6/22

* The best-fit parameters for (1) interstellar photo-electric absorption N_{H} (cm^{−2}), (2) plasma temperature $k_{\text{B}}T^{(\text{GH})}$ (keV), (3) 0.5–2.0 keV surface brightness $S^{(\text{GH})}$ (erg s^{−1} cm^{−2} str^{−1}) of the Galactic halo, (4) 2.0–10.0 keV surface brightness $S^{(\text{CXB})}$ (erg s^{−1} cm^{−2} str^{−1}) of the CXB, (5) χ^2 value and the degree of freedom.

† The error ranges indicate 1 σ statistical uncertainty. The values without errors are those fixed during the fitting.

Table 4. Fitting results for the lobe spectrum.

	— Galactic halo —		— CXB —		— Thermal —		$\chi^2/\text{d.o.f.}$
	$k_{\text{B}}T^{(\text{GH})}$	$S^{(\text{GH})}/10^{-8}$	$S^{(\text{CXB})}/10^{-8}$	$k_{\text{B}}T^{(\text{lobe,T})}$	$S^{(\text{lobe,T})}/10^{-8}\ddagger$		
	(keV)	($\text{erg s}^{-1} \text{cm}^{-2} \text{str}^{-1}$)		(keV)	($\text{erg s}^{-1} \text{cm}^{-2} \text{str}^{-1}$)		
	(1)	(2)	(3)	(4)	(5)		(6)
Without NT	0.20 ^{+0.01} _{-0.01}	1.36 ^{+0.07} _{-0.07}	8.17 ^{+0.12} _{-0.12}	0.99 ^{+0.01} _{-0.01}	1.90 ^{+0.06} _{-0.06}		426.4/319
With NT	0.19 ^{+0.01} _{-0.01}	1.28 ^{+0.07} _{-0.07}	5.85 ^{+0.12} _{-0.12}	0.98 ^{+0.02} _{-0.02}	1.78 ^{+0.06} _{-0.06}		395.9/319

* The best-fit parameters for the fitting with and without the lobe non-thermal (NT) component in the model. The parameters are (1) plasma temperature (2) 0.5–2.0 keV surface brightness of the Galactic halo, (3) 2.0–10.0 keV surface brightness of the CXB, (4) plasma temperature, (5) 0.5–2.0 keV surface brightness of the lobe thermal emission, and (6) χ^2 value and the degree of freedom. The photo-electric absorption column density was fixed to $2.06 \times 10^{20} \text{ cm}^{-2}$, while the power-law index and the surface brightness of the non-thermal component was fixed to 1.68 and $2.0 \times 10^{-8} \text{ erg s}^{-1} \text{ cm}^{-2} \text{ str}^{-1}$ in the 2.0–10.0 keV band.

† The error ranges indicate 1σ statistical uncertainty.

‡ A uniform distribution over a $12'$ radius disk was assumed.

3.3.2.1. Point-like sources In order to see the contribution by point-like sources, we utilized the XMM-Newton data, which has much better X-ray optics, hence is more sensitive to point-like sources. We started with the XMM-Newton source list in the pipeline products with a detection significance above 5σ . For each individual source, we accumulated source and background events from a $36''$ radius circle and a 72 – $180''$ annulus, respectively. In the background annulus, $36''$ radius circles around other sources were masked. The RMF and ARF were generated using the `rmfgen` and `arfgen` tools.

We constructed the composite spectrum of all the XMM-Newton point-like sources except for XMMU J032112.4–370337, and fitted it successfully with an absorbed power-law model with the best-fit photon index of $2.22^{+0.04}_{-0.03}$ and the surface brightness of $2.57^{+0.16}_{-0.15} \times 10^{-8} \text{ erg s}^{-1} \text{ cm}^{-2} \text{ str}^{-1}$ in 2.0–10.0 keV band, assuming that the summed flux is distributed uniformly across the lobe region. We do not include this component in the model to fit the XIS spectrum to avoid a duplicated count with the CXB emission, which is mostly the ensemble of such point-like sources of background AGNs (Giacconi et al. 2001). We also confirmed that there is no local excess of point-like source populations in the lobe region by comparing with the XMM-Newton source list constructed in one of the comparison regions (sequence ID 703038010 in table 2). A somewhat softer spectrum of the composite point-like sources in comparison with the CXB may be due to contamination by the diffuse thermal emission into the apertures around each source. Anyway, the surface brightness of the point-like sources is only about 1/10 of that of the lobe thermal emission at 1 keV. We thus conclude that the ensemble of point-like sources does not account for the observed excess emission in the lobe region.

3.3.2.2. Non-thermal emission Following the previous work (Tashiro et al. 2009), we further added the lobe non-thermal component originating from inverse Compton emission to the model. The photon index and the surface brightness were fixed to 1.68 and $2.0 \times 10^{-9} \text{ erg s}^{-1} \text{ cm}^{-2} \text{ str}^{-1}$ in the 2.0–10.0 keV band (Tashiro et al. 2009). The fitting improved slightly with little changes in the best-fit parameters of the lobe ther-

mal component (table 4). We thus conclude that the lobe thermal emission is present regardless of whether or not we include the lobe non-thermal component in the model.

3.3.2.3. Galaxy component Kim et al. (1998) and Kim & Fabbiano (2003) revealed, using the high-resolution X-ray imagers on-board the ROSAT and Chandra X-ray Observatory respectively, that diffuse X-ray emission exists around NGC 1316 in smoothed X-ray images after removing point-like sources. The morphology of the diffuse emission is elongated in the direction normal to the jet launching direction at its root. The extent of the diffuse emission is quite limited; the brightness drops by an order of magnitude in $10''$ in the radial profile (see figure 6 in Kim & Fabbiano 2003). The spectrum was modeled with a thermal plasma with a temperature of $k_{\text{B}}T = 0.5$ – 0.6 keV.

Konami et al. (2010) used the same XIS data presented here (sequence ID 801015010 in figure 1) to analyze the X-ray spectrum of the diffuse emission in NGC 1316. Despite the limited imaging capability of Suzaku, they identified the spectrum of the diffuse plasma emission with its most prominent features of Mg XI and Si XIII emission lines. These features are absent in their background region taken from $5'$ away from the center of the galaxy, for which the spectrum was explained only by background emission. The lobe region is separated from NGC 1316 by $\sim 8'$ so we can safely assume that our diffuse X-ray spectrum in the lobe is free from contamination by the galaxy component.

3.4. Spatial Extent of the Thermal Emission

Finally, we investigated the spatial distribution of the lobe thermal emission. We divided the regions inside and outside of the lobe radially into three elliptical annuli (R2–R4; figure 2b). Here, R3+R4 is the lobe region used for the analyses in the previous sections. We also defined the R1 region as a concentric ellipse outside of the R2 region and within the field of the sequence ID = 804036010 (figure 1), which is intended to examine the local background unaffected by the central galaxy and the eastern lobe. For each region, we conducted spectral modeling in the same approach as in § 3.3.1. The results are shown in figure 5.

We compared the observed radial profile with the projected profile calculated by assuming that the thermal gas

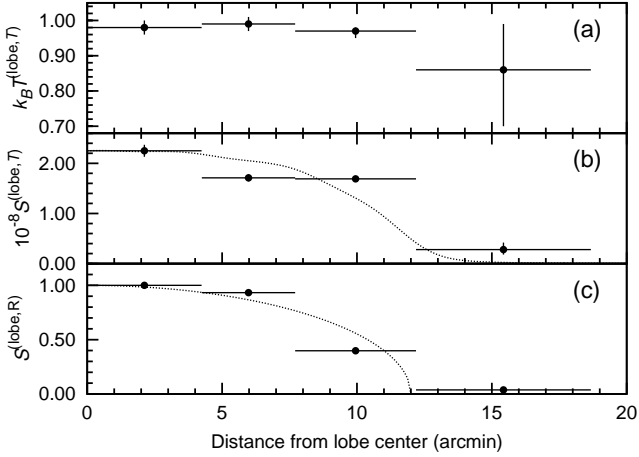


Fig. 5. Radial profiles of (a) the plasma temperature ($k_B T^{(\text{lobe},T)}$) and (b) the surface brightness $S^{(\text{lobe},T)}$ of the diffuse thermal emission, and (c) the 1.5 GHz total intensity (Fomalont et al. 1989) from the center of the western lobe. The horizontal error bars are the region size calculated as the logarithmic mean of the major and minor axes of the ellipses (R1–R4; figure 2b), while the vertical error bars correspond to 1σ statistical uncertainty. The curves in (b) and (c) show the fully-resolved (c) and PSF-convolved (b) radial profiles of completely optically-thin emission from a uniformly filled sphere of $12'$ radius.

is optically thin and uniformly fills a spherical volume with a radius of $12'$ (the approximate size of the western lobe as seen in the 1.5 GHz radio band; figure 2) around the center of the western lobe at (RA, DEC) = ($03^{\text{h}}21^{\text{m}}29^{\text{s}}$, $-37^{\circ}07'52''$) in the equinox J2000.0. The dashed curve in figure 5 (c) shows the case when the spatial distribution is fully resolved, while that in figure 5 (b) shows the case when the distribution is convolved with the point spread function of the XIS. The observed profile of the thermal X-ray emission is consistent with the assumed distribution, and there is no indication of relative enhancement toward the outer edges of the lobe that would suggest a shell-like structure.

4. Discussion

Our Suzaku observations have confirmed the presence of the diffuse thermal emission in the western lobe of For A. We argued that this emission is local to the lobe, unlike those from the Galactic halo, CXB, and Fornax cluster gas, because it is not found in the three comparison regions (§ 3.2). We also argued that the emission cannot be explained by the ensemble of point-like sources, the non-thermal emission in the lobe, nor the contaminating hot gas from the NGC 1316 galaxy (§ 3.3). The surface brightness distribution is consistent with optically-thin plasma emission of a uniform spherical distribution whose position and extent are comparable to those observed in the radio band (§ 3.4).

In view of evidence for thermal plasma residing within the lobe, we estimate its physical attributes such as the pressure and energy balance, as well the total mass and

energy. The best-fit APEC normalization N_{APEC} is related to the electron density n_e as

$$4\pi D^2(1+z)^2 \times 10^{14} N_{\text{APEC}} = n_e^2 V f, \quad (1)$$

where D is the distance to For A (18.6 Mpc), z is the redshift (4.65×10^{-3}), V is the western lobe volume, and f is the volume filling factor. We assume for simplicity that the plasma consists only of ionized H and electrons. For the emitting volume fV , we consider a uniform sphere with an angular radius of $\theta = 12'$ (figure 5), so that $V = 4\pi(D\theta)^3/3$. Using the best-fit values from spectral fitting in table 4, we derive the electron density $n_e = 3.0 \times 10^{-4} f^{-1/2} \text{ cm}^{-3}$, the thermal gas pressure $p_T = 2n_e k_B T f^{-1/2} = 1 \times 10^{-12} f^{-1/2} \text{ erg cm}^{-3}$, the total thermal energy $E_T = 3n_e k_B T fV \sim 5 \times 10^{58} f^{1/2} \text{ erg}$, and the total gas mass $M_T = m_p n_e fV \sim 9 \times 10^9 f^{1/2} M_\odot$, where m_p is the proton mass. The filling factor is constrained to be $f^{1/2} > 10^{-3}$, as the radiative cooling time of the gas $\tau_{r,c} \sim E_T/L_T \approx 10^3 f^{1/2} \text{ Gyr}$ must not be shorter than the radio lobe's age of 0.1 Gyr (Iyomoto et al. 1998), where $L_T \sim S^{(\text{lobe},T)}(D(1+z)\theta)^2$ is the thermal X-ray luminosity.

A comparison of the energy densities in the thermal gas ϵ_T , in the magnetic field ϵ_{mag} and in non-thermal electrons $\epsilon_{\text{NT},e}$ is shown in table 5. Tashiro et al. (2009) derived $\epsilon_{\text{mag}} = 6.7 \times 10^{-14} \text{ erg cm}^{-3}$ and $\epsilon_{\text{NT},e} = 5.0 \times 10^{-13} \text{ erg cm}^{-3}$ under the assumption that the observed radio and X-ray emission are respectively due to synchrotron radiation in a homogeneous magnetic field and inverse Compton upscattering of cosmic microwave background photons. If the volume filling factor is unity for all components, $\epsilon_T/\epsilon_{\text{NT},e} \sim 3$, so the thermal plasma is not far from energy equipartition with the non-thermal electrons, even though ϵ_{mag} is about an order of magnitude smaller than either of the other two.

As mentioned in § 3.2.2, the thermal emission from the ICM of the Fornax cluster is not directly observable in the vicinity of For A. In order to examine the pressure balance between the For A lobe and the ambient ICM, we must rely on extrapolations from the properties of the ICM observed in the inner regions by Jones et al. (1997). For the electron density, the beta-model profile determined at cluster radii 35–280 kpc is extrapolated to the position of For A at ~ 1500 kpc. Although the temperature profile was seen to be declining with radius, the value of the temperature itself was not well constrained, so we use the outermost observed value of 1.1 keV at 120 kpc as an upper limit at the position of For A. In this manner, the ICM pressure around the For A lobe is estimated to be $\lesssim 2 \times 10^{-13} \text{ erg cm}^{-3}$. The total pressure within the lobe due to the thermal gas, non-thermal electrons and magnetic field is larger than this value by a factor of $\gtrsim 5$, implying that the lobe is over-pressured with respect to the ambient medium, although not by a very large amount.

The above properties of the thermal gas in the For A lobe can be compared with those tentatively identified recently in the giant lobes of the nearby radio galaxy Cen A through two lines of evidence; diffuse thermal X-ray emission, albeit in a small portion of the entire lobe (Stawarz

et al. 2013), and excess Faraday rotation measures in radio polarization maps (O’Sullivan et al. 2013). In contrast to our case here for For A, the two Suzaku pointings by Stawarz et al. (2013) only cover a limited area of Cen A’s southern giant lobe, and the spectra and spatial distribution of the thermal X-ray emission across the lobe is unavailable. Although the polarization maps of O’Sullivan et al. (2013) cover the whole lobe structure, the measured rotation measures are highly non-uniform and their interpretation is complicated by the unknown structure of the magnetic field. Nevertheless, Stawarz et al. (2013) and O’Sullivan et al. (2013) estimated volume-averaged quantities for the thermal gas that are consistent with each other, which are listed in table 5. For the Cen A lobe, ϵ_T , ϵ_{mag} and $\epsilon_{\text{NT,e}}$ all seem to be roughly in equipartition with each other. Although this is unlike For A for which $\epsilon_{\text{mag}} \ll \epsilon_{\text{NT,e}}$, the ratio of energies in the thermal gas relative to the sum of those in the non-thermal components $\epsilon_T/(\epsilon_{\text{mag}} + \epsilon_{\text{NT,e}}) \sim 3$ appears to be similar for both objects. Assuming such gas to be distributed throughout the entire lobe of Cen A, the total estimated mass of $M_T \sim 10^{10} M_\odot$ (O’Sullivan et al. 2013) is also similar to our value for For A.

Finally, we speculate on the origin of the thermal gas inside the For A lobe. Its total mass of $M_T \sim 9 \times 10^9 f^{1/2} M_\odot$ can be compared with the mass of the central black hole $M_{\text{BH}} \sim (1 - 2) \times 10^8 M_\odot$ (Kuntschner 2000), and the total gas mass currently in the host galaxy $M_{\text{g,host}} \sim 3.3 \times 10^9 M_\odot$ (Forman et al. 1985). Assuming a filling factor of unity, $M_T \sim 100 \times M_{\text{BH}}$, which immediately disfavors the possibility that it was transported outward from the nucleus inside the jets, since it is highly improbable that 100 times more mass can be ejected than it can be accreted onto the black hole.

Therefore, the gas must have somehow been transported into the lobe from its surroundings on larger scales. The fact that $M_T \gg M_{\text{BH}}$ also entails that this transport process must inevitably be accompanied by strong deceleration of the outflow. The jet kinetic energy can be written $E_{\text{jet}} = \eta_{\text{jet}} M_{\text{acc}} c^2$, where M_{acc} is the total mass accreted onto the black hole, and η_{jet} is the corresponding efficiency of conversion from rest mass energy. If the jet is loaded with baryonic material with mass M_{jet} from its environs at some location, its bulk Lorentz factor $\Gamma_{\text{jet}} = 1 + E_{\text{jet}}/M_{\text{jet}} c^2 \leq 1 + \eta_{\text{jet}} M_{\text{BH}}/M_{\text{jet}}$, as $M_{\text{acc}} \leq M_{\text{BH}}$. Considering physically plausible values of $\eta_{\text{jet}} < 1$, if $M_{\text{jet}} \sim M_{\text{BH}}$, $\Gamma_{\text{jet}} \lesssim 2$ and the jet must be decelerated to sub-relativistic velocities, as is often invoked to explain the morphological properties of FR I radio galaxies (Bicknell 1995). If $M_{\text{jet}} \gg M_{\text{BH}}$, $\Gamma_{\text{jet}} \rightarrow 1$, and the deceleration is likely to be so severe as to disrupt the robust development of jet structure. Hence, gas with mass as large as M_T cannot have been entrained into the jet during its passage through the interstellar medium (ISM) of the galaxy, as it would preclude the formation of well-defined lobes on much larger scales as observed, even though $M_{\text{g,host}}$ is seen to be comparable to M_T .

Thus, the gas is likely to have been entrained into the

lobe after it has sufficiently expanded and evolved, perhaps after cessation of the jet energy supply, through e.g. Rayleigh-Taylor instabilities in the interface between the lobe and the external medium (Reynolds et al. 2002). The material itself may be either the ambient ICM, or ISM that has been swept up and accumulated outside the lobe (but not entrained) during propagation in the host galaxy. In either case, the implication is that the radio jets and lobes have exerted a profound influence on the gaseous medium of its host galaxy and/or cluster. Further discussion on the origin of the thermal gas must await more detailed observations of this and other objects.

5. Summary

We presented the results of X-ray mapping observations of the western radio lobe of the For A galaxy using the Suzaku XIS. Comparing with the Suzaku data in three near-by regions and XMM-Newton data in the lobe, we concluded that diffuse thermal emission with temperature $k_B T \sim 1$ keV is present in the western part of the lobe in excess of background and contaminating emission. The surface brightness distribution is consistent with a uniform spherical distribution centered within the western lobe with a projected radius of $12'$.

We derived the physical parameters of the thermal gas responsible for the diffuse emission. Its total mass and energy amounts respectively to $\sim 9 \times 10^9 f^{1/2} M_\odot$ and $\sim 5 \times 10^{58} f^{1/2}$ erg. Such a large mass disfavors the possibility that the gas was ejected from the central engine, and instead implies that it was transported into the jet from its surroundings on large scales, a potential indication of significant interaction and feedback of the radio jet with the host galaxy and/or cluster. Some properties, such as the approximate equipartition of the thermal and non-thermal components and the total gas mass appear to be similar to the thermal gas tentatively found in the giant lobe of the Cen A radio galaxy. Future, more detailed studies, particularly of the spatial distribution of such emission components in For A and other radio galaxies are warranted to elucidate its origin and its implications.

We acknowledge N. Isobe for useful discussion. H.S. is supported by the Research Center for Measurement in Advanced Science in Rikkyo University. MST and SI are supported in part by the Grants-in-Aid for Scientific Research Nos. 22340039 and 22540278 from MEXT of Japan, respectively. This research made use of data obtained from Data ARchives and Transmission System (DARTS), provided by Center for Science-satellite Operation and Data Archives (C-SODA) at ISAS/JAXA.

References

- Abdo, A. A., Ackermann, M., Ajello, M., et al. 2010, *Science*, 328, 725
- Anders, E. & Grevesse, N. 1989, *Geochim. Cosmochim. Acta*, 53, 197

Table 5. Physical parameters of the For A and Cen A lobes.

Object	n_e (cm^{-3}) (1)	$k_B T$ (keV) (2)	V (cm^3) (3)	ϵ_T (erg cm^{-3}) (4)	ϵ_{mag} (erg cm^{-3}) (5)	$\epsilon_{\text{NT,e}}$ (erg cm^{-3}) (6)	R (7)
For A [†]	3.0×10^{-4}	1.0	3.4×10^{70}	1.4×10^{-12}	6.7×10^{-14}	5.0×10^{-13}	2.5
Cen A [‡]	$0.9\text{--}2.5 \times 10^{-4}$	0.5	2.0×10^{71}	2.4×10^{-13}	4.0×10^{-14}	5.2×10^{-14}	2.6

* The parameters are (1) electron density, (2) temperature, and (3) emitting volume (cm^3) assuming a volume filling factor of unity for the lobe thermal emission. The energy densities of (4) the thermal emission, (5) magnetic field, and (6) non-thermal electrons. (7) The ratio of energies in thermal to non-thermal components defined as $\epsilon_T/(\epsilon_{\text{mag}} + \epsilon_{\text{NT,e}})$.

[†] The values are from this work and Tashiro et al. (2009).

[‡] The values are from Stawarz et al. (2013); Abdo et al. (2010).

- Begelman, M. C., Blandford, R. D., & Rees, M. J. 1984, *Reviews of Modern Physics*, 56, 255
- Bicknell, G. V. 1995, *ApJS*, 101, 29
- Ekers, R. D., Goss, W. M., Wellington, K. J., et al. 1983, *A&A*, 127, 361
- Feigelson, E. D., Laurent-Muehleisen, S. A., Kollgaard, R. I., & Fomalont, E. B. 1995, *ApJL*, 449, L149
- Fomalont, E. B., Ebner, K. A., van Breugel, W. J. M., & Ekers, R. D. 1989, *ApJL*, 346, L17
- Forman, W., Jones, C., & Tucker, W. 1985, *ApJ*, 293, 102
- Giacconi, R., Rosati, P., Tozzi, P., et al. 2001, *ApJ*, 551, 624
- Harris, D. E. & Krawczynski, H. 2006, *ARA&A*, 44, 463
- Ishisaki, Y., Maeda, Y., Fujimoto, R., et al. 2007, *PASJ*, 59, 113
- Isobe, N., Makishima, K., Tashiro, M., et al. 2006, *ApJ*, 645, 256
- Isobe, N., Tashiro, M. S., Gandhi, P., et al. 2009, *ApJ*, 706, 454
- Iyomoto, N., Makishima, K., Tashiro, M., et al. 1998, *ApJL*, 503, L31
- Jansen, F., Lumb, D., Altieri, B., et al. 2001, *A&A*, 365, L1
- Jones, C., Stern, C., Forman, W., et al. 1997, *ApJ*, 482, 143
- Kalberla, P. M. W., Burton, W. B., Hartmann, D., et al. 2005, *A&A*, 440, 775
- Kaneda, H., Tashiro, M., Ikebe, Y., et al. 1995, *ApJL*, 453, L13
- Kim, D.-W. & Fabbiano, G. 2003, *ApJ*, 586, 826
- Kim, D.-W., Fabbiano, G., & Mackie, G. 1998, *ApJ*, 497, 699
- Kokubun, M., Makishima, K., Takahashi, T., et al. 2007, *PASJ*, 59, 53
- Konami, S., Matsushita, K., Nagino, R., et al. 2010, *PASJ*, 62, 1435
- Koyama, K., Tsunemi, H., Dotani, T., et al. 2007, *PASJ*, 59, 23
- Kuntschner, H. 2000, *MNRAS*, 315, 184
- Kushino, A., Ishisaki, Y., Morita, U., et al. 2002, *PASJ*, 54, 327
- Lanz, L., Jones, C., Forman, W. R., et al. 2010, *ApJ*, 721, 1702
- Lumb, D. H., Warwick, R. S., Page, M., & De Luca, A. 2002, *A&A*, 389, 93
- Madore, B. F., Freedman, W. L., Silbermann, N., et al. 1999, *ApJ*, 515, 29
- McNamara, B. R. & Nulsen, P. E. J. 2007, *ARA&A*, 45, 117
- McNamara, B. R. & Nulsen, P. E. J. 2012, *New Journal of Physics*, 14, 055023
- Mitsuda, K., Bautz, M., Inoue, H., et al. 2007, *PASJ*, 59, 1
- Nulsen, P., Panagoulia, E., Kraft, R., et al. 2011, in *AAS/High Energy Astrophysics Division*, Vol. 12, AAS/High Energy Astrophysics Division, 46.03
- O’Sullivan, S. P., Feain, I. J., McClure-Griffiths, N. M., et al. 2013, *ApJ*, 764, 162
- Panagoulia, E., Nulsen, P., Kraft, R., et al. 2011, in *Bulletin of the American Astronomical Society*, Vol. 43, American Astronomical Society Meeting Abstracts #217, 142.18
- Reynolds, C. S., Heinz, S., & Begelman, M. C. 2002, *MNRAS*, 332, 271
- Serlemitsos, P. J., Soong, Y., Chan, K., et al. 2007, *PASJ*, 59, 9
- Smith, R. K., Brickhouse, N. S., Liedahl, D. A., & Raymond, J. C. 2001, *ApJL*, 556, L91
- Stawarz, L., Tanaka, Y. T., Madejski, G., et al. 2013, *ApJ*, 766, 48
- Strüder, L., Briel, U., Dennerl, K., et al. 2001, *A&A*, 365, L18
- Takahashi, T., Abe, K., Endo, M., et al. 2007, *PASJ*, 59, 35
- Tashiro, M., Makishima, K., Iyomoto, N., Isobe, N., & Kaneda, H. 2001, *ApJL*, 546, L19
- Tashiro, M. S., Isobe, N., Seta, H., Matsuta, K., & Yaji, Y. 2009, *PASJ*, 61, 327
- Tawa, N., Hayashida, K., Nagai, M., et al. 2008, *PASJ*, 60, 11
- Turner, M. J. L., Abbey, A., Arnaud, M., et al. 2001, *A&A*, 365, L27
- Yoshino, T., Mitsuda, K., Yamasaki, N. Y., et al. 2009, *PASJ*, 61, 805